Experimental study of the structural and magnetic properties of γ-Fe$_2$O$_3$ nanoparticles

S. M. Yusuf,[1,2,*] J. M. De Teresa,[1] M. D. Mukadam,[2] J. Kohlbrecher,[3] M. R. Ibarra,[1,4] J. Arbiol,[5]
P. Sharma,[6] and S. K. Kulshreshtha[6]

[1]*Instituto de Ciencia de Materiales de Aragón, Universidad de Zaragoza-CSIC, Zaragoza 50009, Spain*
[2]*Solid State Physics Division, Bhabha Atomic Research Centre, Mumbai 400 085, India*
[3]*Laboratory for Neutron Scattering, ETHZ &PSI, CH-5232 Villigen PSI, Switzerland*
[4]*Instituto de Nanociencia de Aragón, Universidad de Zaragoza, Zaragoza 50009, Spain*
[5]*TEM-MAT, Serveis Cientificotecnics, Universitat de Barcelona, Barcelona, Spain*
[6]*Chemistry Division, Bhabha Atomic Research Centre, Mumbai 400 085, India*

Structural and magnetic properties of γ-Fe$_2$O$_3$ nanoparticles annealed at 200 and 250 °C have been studied by using high resolution transmission electron microscopy (TEM), electron energy loss spectroscopy, x-ray diffraction, neutron diffraction, polarized small angle neutron scattering (SANS) and dc magnetization techniques. Here we have dealt with an important problem of the symmetry of crystal structure of γ-Fe$_2$O$_3$ nanoparticles with cation vacancy distribution. Present study also correlates various structural and magnetic results that have been obtained for γ-Fe$_2$O$_3$ nanoparticles using various experimental techniques. Analysis of x-ray and neutron diffraction data shows cation vacancies at the octahedral site, consistent with the space group P4$_3$ 3 2. A log-normal distribution of particle size for both the samples has been found. A good crystallinity has been found from TEM, x-ray diffraction and neutron diffraction studies. Neutron diffraction study at room temperature confirms a ferrimagnetic ordering of tetrahedral and octahedral site moments with a net moment of ~1.58 and 1.83 μ_B per formula unit for the samples annealed at 200 and 250 °C, respectively. SANS data analysis is consistent with a mass fractal spatial arrangement of these nanoparticles with a fractal dimension of 1.25. The SANS results are consistent with the same form factor for both the chemical particle size and the magnetic particle size indicating the absence of any observable shell with disordered spins. Superparamagnetic behavior of noninteracting nanoparticles with a log-normal distribution of blocking temperature (with a particle moment of ~28 000 μ_B for the sample annealed at 200 °C) is found in our dc magnetization study at room temperature.

I. INTRODUCTION

The reduction of the grain size of magnetic materials to the nanometric scale has opened, in the last decades, new perspectives in materials science. Nano-sized materials possess unique properties, which are intermediate between the molecular level and the properties of the corresponding bulk materials. Studies of magnetic properties of nanoparticles are of valuable interest from both fundamental and technological point of views. In particular, nanoparticles based on ferromagnetic and/or ferrimagnetic materials are of high scientific interest due to their possible wide technological applications such as in high density magnetic recording media,[1] permanent magnets,[2] magnetic sensors,[3] magnetic refrigerant,[4] ferrofluids,[5] catalysts,[6] and biomedical applications.[7,8] In this study, we investigate nanoparticles of maghemite, γ-Fe$_2$O$_3$. Maghemite is a well-known iron oxide which basically crystallizes in the cubic spinel structure and it can be considered as Fe^{II} deficient magnetite with formula (Fe^{III})$_A$[Fe$^{III}_{5/3}\square_{1/3}$]$_BO_4$. A represents a tetrahedral site, B an octahedral site, and $\square$ a cationic vacancy on the octahedral site.[9] γ-Fe$_2$O$_3$ is the fully oxidized form of magnetite Fe$_3$O$_4$ In the bulk phase, γ-Fe$_2$O$_3$ is used as a recording medium in cassette tapes and disc drives due to its suitable magnetic properties. The demand of higher memory density in information storage media constitutes an important motivation for the fabrication of smaller and smaller particles of γ-Fe$_2$O$_3$.

Also, these γ-Fe$_2$O$_3$ nanoparticles are potentially useful in biomedical applications due to their large magnetic moment. Nanoparticles of γ-Fe$_2$O$_3$ also can have enhanced catalytic properties, compared to the bulk counterpart. Therefore, a growing attention has been devoted to the synthesis and physical properties of γ-Fe$_2$O$_3$ nanoparticles.[10,11]

A relatively large value of magnetization has been reported in the literature for nearly defect-free γ-Fe$_2$O$_3$ nanocrystallites.[12] However, no detailed quantitative structural analysis was given in that study. In fact, in the literature controversial results of crystal structure of γ-Fe$_2$O$_3$ are reported.[9,13–15] γ-Fe$_2$O$_3$ being a very important material with wide commercial and industrial applications, the knowledge of microstructure of this material is the subject of much interest. It is therefore necessary to know the structural details in the nanoparticles of γ-Fe$_2$O$_3$ using various structural characterization techniques. Cation distributions (and cation vacancies) in the A and B sites at the core of nanoparticles are crucial parameters in this regard. The physical properties of such nanoparticles are governed by their size, shape, and surface effects. Other important parameters are the particle size distribution and interparticle magnetic correlations. Therefore, a quantitative study of intertwined structural and physical (magnetic) properties of γ-Fe$_2$O$_3$ nanoparticle systems is necessary. Investigations of particle size and its distribution using various advanced techniques and their role in establishing magnetic properties (field dependence of dc magnetization and blocking temperature distribution, etc.)

are very important in the area of nanoscience and nanotechnology. For practical applications of γ-Fe_2O_3 nanoparticles, it is required to have high magnetization with low saturation-magnetic-field with possible smallest size of nanoparticles. The magnetic behavior is particularly complex in powder solid samples with nanoparticles in close contact. It is therefore, quite important to understand the effects of these parameters on magnetic properties of such nanoparticles. In view of this we have prepared γ-Fe_2O_3 nanoparticles (in solid powder form) using a reverse micelle technique and studied their structural and magnetic properties in detail. Here we present the results of our small angle neutron scattering (SANS) study using polarized beam and dc magnetization measurements on two nanoparticle samples of γ-Fe_2O_3 which are well characterized by x-ray diffraction, neutron diffraction, and transmission electron microscopy (TEM) techniques. Using these techniques a consistent view of structural and magnetic properties incorporating the distribution of particle size is given. Present study deals with γ-Fe_2O_3 nanoparticles with strong ferrimagnetic character at room temperature which make them suitable for practical applications.

II. EXPERIMENT

The sample of γ-Fe_2O_3 was precipitated in fine water droplets by using the principle of reverse micelles.[16] For this purpose, a stock solution 0.5 M Bis (2-ethylhexyl) sodium sulfosuccinate (AOT) was prepared in hexane and to this solution 0.2 M Fe^{3+} and 0.1 M Fe^{2+} solutions were added in such a way that the water to AOT ratio R ($=[H_2O]/[AOT])=15$ was maintained. Similarly, another solution of NH_4OH was prepared by using liquor ammonia solution of specific gravity 0.91 in such a way that R=15 was maintained. These two micellar solutions were slowly mixed together with continuous stirring. Both Fe^{3+} and Fe^{2+} ions were used to prevent the precipitation of antiferromagnetic $Fe(OH)_3$ phase. Ferric oxide precipitation, occurred in water droplets, was coagulated by adding acetone and centrifuged to separate out the ferric oxide precipitate. This sample was repeatedly washed with water and acetone separately in order to remove the ammonia and AOT, respectively, from this sample. Finally, the sample was dried in an oven at $\sim150\ ^\circ$C for 16 h to remove the water and acetone. The as-prepared sample is then divided in two parts and annealed at two different temperatures, 200 and 250 $^\circ$C, for 16 h and the γ-Fe_2O_3 samples are obtained in solid powder form. We will refer to these samples, annealed at 200 and 250 $^\circ$C, as S200 and S250, respectively.

High-resolution transmission electron microscopy (HRTEM) and electron energy loss spectroscopy (EELS) experiments were performed using a FEG TEM JEOL 2010F instrument operated at an accelerating voltage of 200 kV (point to point resolution 0.19 nm) and Gatan Image Filter 2000 with 0.8 eV energy resolution, respectively. Samples for TEM were prepared on copper grids coated with a carbon support film (Pelco International) by evaporating a drop of particles dispersion. Before taking TEM images at room temperature, the samples, prepared on the carbon support film,

were cleaned on a plasma consisting in 0.5% O in Ar.

The x-ray diffraction measurements were performed on both the samples using Cu $K\alpha$ ($\lambda=1.5418$ Å) radiation over a scattering angular 2θ range of ~10–$120°$ covering a Q $[(4\pi/\lambda)\sin\theta]$ range of 0.710–7.059 Å^{-1} at room temperature. Unpolarized neutron diffraction data were collected at room temperature using the five linear position sensitive detector based powder diffractometer at the Dhruva Reactor, Trombay, India. For neutron diffraction measurements, the samples were placed in a vanadium can and data were collected over the 2θ range of $\sim6°$ to $138°$ in steps of $0.05°$ with a wavelength of 1.249 Å covering a Q range of 0.527–9.393 Å^{-1}.

Small angle neutron scattering using polarized incident beam was carried out using the SANS-I instrument at Paul Scherrer Institute, Switzerland. The I^+ and I^- scattered intensities, with two incident neutron beam polarization states by keeping the spin flipper off and on, respectively, have been measured at 297 K without doing any polarization analysis of the scattered neutrons. Powder samples of γ-Fe_2O_3 were mounted in an Al sample holder of 10 mm inner diameter. In order to avoid multiple scattering, first we carried out test measurements to optimize the thickness of each sample in the beam. A thickness of 0.2 mm was finally used for both the samples for SANS data collection. Measurements were carried out under 0, 0.310, 1.467, and 10.790 kOe horizontal magnetic fields (H) applied perpendicular to the incident neutron beam propagation direction covering a Q range of $\sim0.04\leqslant Q\leqslant2$ nm^{-1} with $\lambda=8$ Å ($\Delta\lambda/\lambda=10\%$) and by placing an x-y detector at a distance of 3, 6, and 15 m from the sample position. The data were corrected in the usual way for transmission, detector efficiency, and background, and were converted to absolute units of cross section with the aid of the spin incoherent scattering of water standard.

The dc magnetization measurements were carried out using a 12 Tesla commercial (Oxford Instruments) Vibrating Sample Magnetometer (VSM) and a 9 Tesla physical property measurement system (Quantum Design) as a function of magnetic field and temperature. For zero-field-cooled magnetization (M_{ZFC}) measurements, the sample was first cooled from room temperature down to 5 K in zero external field. After applying the magnetic field at 5 K, the magnetization was measured in the warming cycle with field on. Whereas, for field-cooled magnetization (M_{FC}) measurements, the sample was cooled in the same field (measuring field in the ZFC case) down to 5 K and M_{FC} was measured in the warming cycle under the same field. Magnetization as a function of applied field was measured at 297 K.

III. RESULTS AND DISCUSSION

Figure 1 shows the TEM images for the γ-Fe_2O_3 powder samples S200 and S250. It confirms the formation of nanoparticles for both the samples. The distribution of particle size has been obtained by assuming a log-normal distribution of the particle diameter D:
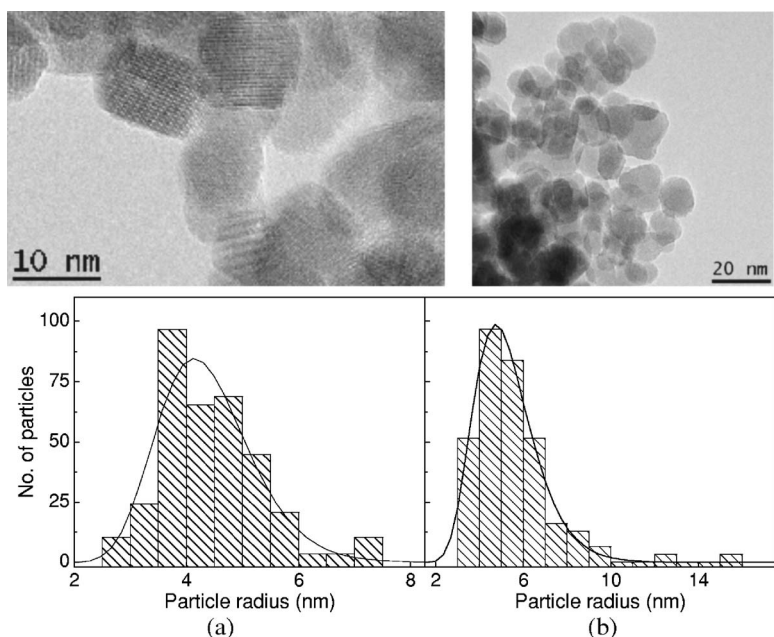
FIG. 1. TEM images and the corresponding number distribution of particle size (diameter) graphs for the (a) 200 and (b) 250 °C annealed γ-Fe$_2$O$_3$ samples.

$$f(D) = \frac{1}{D\sigma_1\sqrt{2\pi}} \exp\left\{-\frac{[\ln(D/D_0)]^2}{2\sigma_1^2}\right\} \quad (1)$$

with median diameter $D_0 = 8.6$ nm and $\sigma_1 = 0.19$ for the S200 sample and $D_0 = 10.17$ nm and $\sigma_1 = 0.27$ for the S250 sample (Fig. 1).

The high-resolution TEM images and the corresponding power spectra, shown in Fig. 2, illustrate the presence of well-defined atomic planes confirming the highly crystalline nature of these nanoparticles. Power spectra shown in Figs. 2(b) and 2(e), could be indexed corresponding to the γ-Fe$_2$O$_3$ crystalline structure. By power spectrum indexation

we observe that the nanoparticles of the S200 sample are aligned along the [2 −2 0] direction [Fig. 2(a)]. Nanoparticles with other alignments are also found (not shown). Figure 2(c) shows an agglomeration along the [1 −1 1] direction for the S250 sample. Similar alignment of nanoparticles in α-Fe$_2$O$_3$ has been reported in the literature.[17] Figure 3 shows EELS data for the S200 sample. The yield analysis confirms the presence of the iron L$_2$ and L$_3$ edge signals and the oxygen K edge signal. The presence of carbon in some parts of the sample is also found only for the S200 sample. The relative content of oxygen and iron in these particles indicates the compositions for Fe$_2$O$_3$ structure (60% O and 40% Fe).

Figure 4 shows the observed and Rietveld refined x-ray diffraction (XRD) patterns for the two samples at room temperature. The observed XRD patterns prove crystalline nature of both samples. Rietveld refinement of the XRD patterns was performed with the FULLPROF program[18] in the WINPLOTR suite of programs. The analysis confirms the γ-Fe$_2$O$_3$ crystalline structure with space group $P4_3 3 2$. Various crystal structural parameters derived from the analysis are given in Tables I and II. The particle diameters of ~11.6±0.1 nm and 11.3±0.2 nm were determined from the
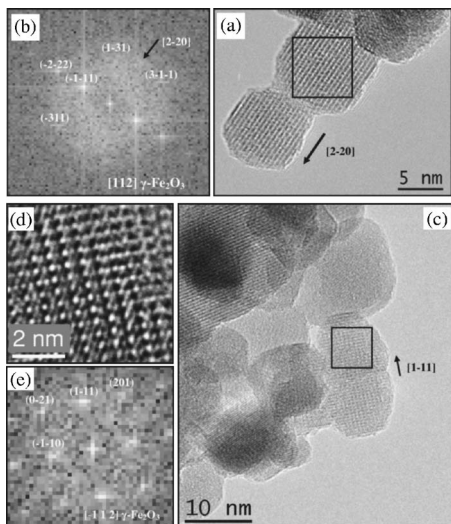

FIG. 2. (a) High resolution TEM image and (b) the corresponding power spectrum taken along the [1 1 2] zone axis in the reciprocal space of the squared region in (a) for the S200 sample. (c) High resolution TEM image, (d) an amplified image of the squared region in (c), and (e) the power spectrum on the same region in (c) taken along the [−1 1 2] zone axis for the S250 sample.
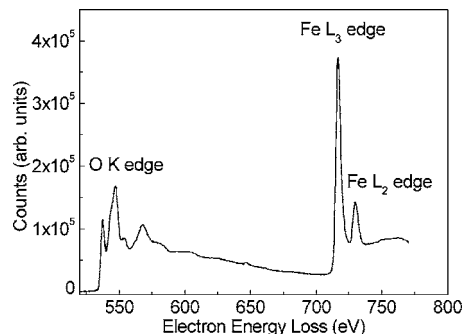

FIG. 3. Background corrected electron energy loss spectroscopy data of the S200 sample.
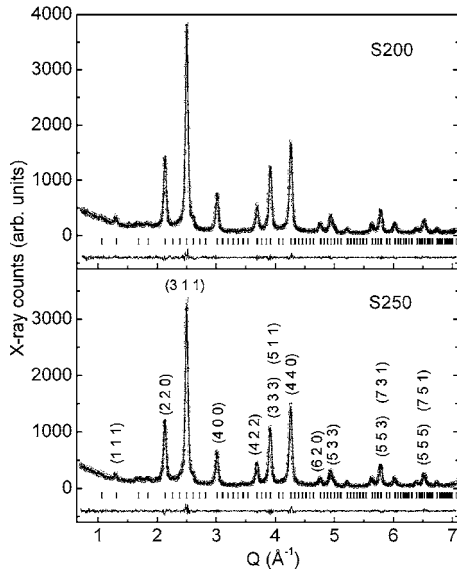
FIG. 4. Observed room-temperature x-ray diffraction patterns of the S200 and S250 samples are shown by open circles. Rietveld refined patterns are shown by solid lines. Solid lines at the bottom of each panel show difference between observed and calculated patterns. The difference patterns are shifted downward for the sake of clarity. The vertical bars indicate the position of allowed Bragg peaks. The (*hkl*) values corresponding to stronger Bragg peaks are also listed.

Y parameter[18] derived from the refinement using the Thompson-Cox Hastings pseudovoid-type Bragg peak shape function.[18] The lattice constants for this cubic structure are found to be 8.3416 (7) and 8.3462 (8) Å for the S200 and S250 samples, respectively.

Figure 5 depicts the observed and Rietveld refined (using the FULLPROF program[18]) neutron powder diffraction patterns at room temperature for both the samples. Rietveld profile analysis technique was used for simultaneous nuclear and magnetic structure refinement. Neutron data analysis demonstrated that the crystal structure could be well refined using $P4_3 3 2$ space group similar to the x-ray diffraction case and the derived structural parameters are consistent with those obtained from the x-ray diffraction data analysis (see Tables I and II). For the S200 sample, the various agreements factors (between the observed and calculated patterns)[18] are found to be $R_p=3.66$, $R_{wp}=4.58$, $R_{exp}=3.57$, and $\chi^2=1.65$.

TABLE I. Structural parameters of the S200 sample at 297 K derived from x-ray diffraction study.

Space group $= P 4_3 3 2$, $a=8.3416$ (7) Å

Atoms	x	y	z	Occupancy
Fe$_{Tetra}$	0.9968 (3)	0.9968 (3)	0.9968 (3)	0.8
Fe$_{Octa1}$	0.8692 (3)	0.6192 (3)	0.8750	1.083 (2)
Fe$_{Octa2}$	0.3750	0.1250	0.8750	0.250 (2)
O1	0.384 (1)	0.384 (1)	0.384 (1)	0.8
O2	0.372 (1)	0.366 (8)	0.874 (1)	2.4

$Rp=5.22$, Rwp$=7.21$, R exp$=6.76$, $\chi^2=1.15$

TABLE II. Structural parameters of the S250 sample at 297 K derived from x-ray diffraction study.

Space group $= P 4_3 3 2$, $a=8.3462$ (8) Å

Atoms	x	y	z	Occupancy
Fe$_{Tetra}$	0.9980 (3)	0.9980 (3)	0.9980 (3)	0.8
Fe$_{Octa1}$	0.8682 (2)	0.6182 (2)	0.8750	1.103 (2)
Fe$_{Octa2}$	0.3750	0.1250	0.8750	0.230 (2)
O1	0.385 (1)	0.385 (1)	0.385 (1)	0.8
O2	0.3714 (8)	0.3703 (8)	0.873 (1)	2.4

$Rp=5.70$, Rwp$=7.90$, R exp$=7.36$, $\chi^2=1.15$

For the S250 sample, these values are $R_p=1.90$, $R_{wp}=2.38$, $R_{exp}=3.18$, and $\chi^2=0.559$. Inset of Fig. 5 depicts the observed pattern and the nuclear part of the calculated diffraction pattern over the lower Q region for the S250 sample. It clearly indicates that the magnetic intensities at lower Q region [for the (1 1 1), (2 2 0), (2 2 2), (4 0 0), and (3 3 1) fundamental Bragg reflections] are quite strong. Similarly for the S200 sample, the presence of strong magnetic Bragg intensities has also been found (not shown in the figure). A ferrimagnetic ordering of tetrahedral and octahedral site moments[9] with a net site averaged ordered moment of 4.15 ± 0.08 and 3.75 ± 0.07 μ_B per Fe ion corresponding to the tetrahedral and octahedral sites, respectively, is found for the S200 sample (Table III). This gives a net moment of ~1.58 μ_B per formula unit. For the S250 sample, the corre-
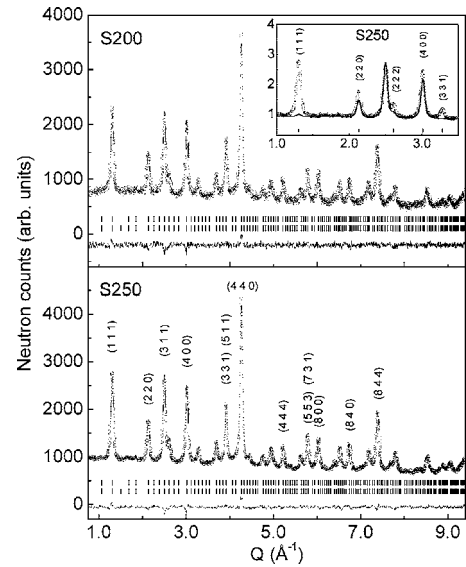

FIG. 5. Observed (open circles) and Rietveld refined (solid lines) neutron diffraction patterns at 297 K. Difference between observed and calculated patterns is also shown by solid lines at the bottom of each panel. The difference patterns are shifted downward for the sake of clarity. The vertical bars indicate the position of allowed Bragg peaks. The (*hkl*) values for stronger Bragg peaks are also listed. Inset shows the observed pattern and the nuclear part of the calculated diffraction pattern over the lower Q region for the S250 sample highlighting the presence of stronger magnetic scattering.

TABLE III. The tetrahedral and octahedral site-averaged ordered moment per Fe ion and a net ordered moment per formula unit derived from the neutron diffraction patterns for γ-Fe_2O_3 nanoparticle samples at room temperature.

Sample	Site-averaged ordered moment			
	Fe 8d-tetra (μ_B)	Fe 12d-octa (μ_B)	Fe 4b-octa (μ_B)	Net moment (μ_B)
S200	4.15	3.75	3.75	1.58
S250	4.06	3.90	3.90	1.83

sponding site moments are found to be 4.06±0.06 and 3.90±0.05 μ_B, with a net moment of ~1.83 μ_B per formula unit. The ordered Fe moment was found to align along the cubic unit cell axes. For the magnetic part of the refinement, a free ion form factor for Fe^{3+} ions at both tetrahedral and octahedral sites is used. The particle (grain) diameters as well as magnetic domain sizes for S200 and S250 samples have been estimated to be ~11.6±0.8 nm and 11.2±0.5 nm, respectively. These values have been estimated from the Y parameters, as already described for the case of x-ray diffraction study. The estimated particle diameters are in good agreement with those obtained from the x-ray diffraction data refinements. It is evident that there is a discrepancy in particle size determined from x-ray/neutron diffraction and TEM techniques. It is known that TEM provides the most accurate information on the particle size with its distribution, whereas x-ray and neutron diffraction study gives the average particle size. The Bragg peaks in x-ray and neutron diffraction patterns are observed due to crystallinity of the sample, hence it is expected that a higher weight factor comes from larger crystallites. Also in the XRD and neutron diffraction study, the particle size has been determined using the Y parameter, derived from the Rietveld refinement with a simplified model.[18] These could be the reason for the derived size discrepancy.

Our analysis of x-ray and neutron diffraction data shows that the crystal structure of γ-Fe_2O_3 maghemite is closely related to that of Fe_3O_4 magnetite (inverse spinel, space group Fd-3m), but differs from the latter by the presence of vacancies distributed on the octahedral sublattice. The Fe^{3+} ions occupy two sublattices (tetrahedral and octahedral) with different coordination with O^{2-} ions. Each unit cell consists of 8 tetrahedral and 16 octahedral sites. However, 1/6 of the octahedral sites are vacant sites (with respect to the Fe_3O_4 structure) as evident from the analysis of the present x-ray as well as neutron diffraction patterns (see Tables I and II). Our data analysis confirms that there are two octahedral sites (12d and 4b) with 9.75% and 37.5% cation vacancies at the 12d and 4b octahedral sites, respectively, for the S200 sample. The corresponding values for the S250 sample are 8.08% and 42.5%. Refinement does not show any vacancy at the 8c tetrahedral site. The ratio of total cation and oxygen occupancies is found to maintain the ideal 2:3 corresponding to γ-Fe_2O_3 for both the S200 and S250 samples. The tetrahedral sublattice has higher coordination with O^{2-} ions than the octahedral sublattice. The tetrahedral site has four nearest

neighbors in tetrahedral sublattices and 12 in octahedral sublattices, whereas, the octahedral site has six nearest neighbors in tetrahedral sublattices and six in octahedral sublattices. Since γ-Fe_2O_3 has inherent one-sixth cation vacancies $\square$ in the octahedral sublattice according to the formula $4Fe_2O_3 \rightarrow 3\{Fe^{3+}O \cdot (Fe^{3+}_{5/3}\square_{1/3})O_3\}$, depending upon the sample preparation method, the different degree of order-disorder at different sublattices is possible.[9,19] In the present study we find that the structure of γ-Fe_2O_3 is cubic corresponding to space group $P4_3 3 2$. The crystal structure could have a more complex ordering with another space group due to vacancy ordering which would give rise to weak superstructure peaks in the diffraction patterns.[19] The space group $P4_32_12$ was found to identify the lattice symmetry with the formation of the threefold unit cell with $a' = b' = a$ and $c' \approx 3a$, where a', b', c', and a are the tetragonal and cubic lattice constants, respectively,[9] but the detailed structural description has not yet been provided.

With an aim to determine the size and size-distribution of the chemical as well as magnetic particles we present the results of our polarized SANS study. This polarized SANS mode (as compared to unpolarized neutron SANS) is expected to determine magnetic form factor more accurately due to the presence of interference term between nuclear and magnetic scattering amplitudes.[20–23] Before presenting the results, first we briefly describe the theory of polarized SANS that is relevant for the present study. The scattered SANS intensities $I(Q)^{\pm}$ for the "+" (spin flipper off) and "−" (spin flipper on) states of the incident beam polarization, respectively, are proportional to the differential scattering cross section $d\sigma/d\Omega^{\pm}$ (Refs. 20 and 21) where

$$\frac{d\sigma}{d\Omega}^{\pm}(\mathbf{Q}) = [F_N^2(\mathbf{Q}) \mp 2F_N(\mathbf{Q})F_M(\mathbf{Q})\sin^2\alpha$$
$$+ F_M^2(\mathbf{Q})\sin^2\alpha]S(\mathbf{Q}). \quad (2)$$

The scattering amplitude for nuclear scattering can be expressed as

$$F_N(\mathbf{Q}) = \Delta B_N V f_p(\mathbf{Q}), \quad (3)$$

where ΔB_N is the contrast for nuclear scattering between the particles and the surrounding matrix (air, in the present case), V is the particle volume and $f_p(\mathbf{Q})$ is the particle form factor. For a spherical particle with radius R

$$f_p(QR) = 3\frac{\sin(QR) - QR\cos(QR)}{(QR)^3} \quad (4)$$

and the volume of the particle $V = \frac{4}{3}\pi R^3$. $F_M(\mathbf{Q})$ denotes the scattering amplitude for magnetic scattering which can be expressed as

$$F_M(\mathbf{Q}) = (\gamma e \mu_0/h)\Delta M V f_m(\mathbf{Q}), \quad (5)$$

where the gyromagnetic ratio $\gamma = -1.913$, e is the electronic charge, μ_0 is the permeability of free space, h is the Plank constant, ΔM is the contrast for magnetic scattering between the magnetic particle and the surrounding matrix, and $f_m(\mathbf{Q})$ is the magnetic form factor of the particle. Here $\mathbf{Q}$ is the scattering vector, α is the angle between the applied mag-

netic field H and Q, i.e., the azimuthal angle on the two-dimensional (2D)SANS detector. $S(Q)$ is the structure factor that characterizes the correlations in the spatial distribution of particles. Equation (2) is valid when the applied magnetic field is large enough to saturate the magnetization along the field direction. Equation (2) can be written as

$$\frac{d\sigma^+}{d\Omega} = \frac{d\sigma^+}{d\Omega}_{\text{iso}} + \frac{d\sigma^+}{d\Omega}_{\text{aniso}} \sin^2 \alpha \qquad (6)$$

and

$$\frac{d\sigma^-}{d\Omega} = \frac{d\sigma^-}{d\Omega}_{\text{iso}} + \frac{d\sigma^-}{d\Omega}_{\text{aniso}} \sin^2 \alpha, \qquad (7)$$

where the isotropic differential scattering cross section terms are same in both $d\sigma/d\Omega^+$ and $d\sigma/d\Omega^-$ and they can be expressed as

$$\frac{d\sigma^\pm}{d\Omega}_{\text{iso}} = F_N^2(Q)S(Q). \qquad (8)$$

The anisotropic terms are given as

$$\frac{d\sigma^+}{d\Omega}_{\text{aniso}} = [F_M^2(Q) - 2F_N(Q)F_M(Q)]S(Q) \qquad (9)$$

for the incident $(+)$ spin state and

$$\frac{d\sigma^-}{d\Omega}_{\text{aniso}} = [F_M^2(Q) + 2F_N(Q)F_M(Q)]S(Q) \qquad (10)$$

for the incident $(-)$ spin state. The average of these two anisotropic terms is

$$\left(\frac{d\sigma^+}{d\Omega}_{\text{aniso}} + \frac{d\sigma^-}{d\Omega}_{\text{aniso}} \right) \Big/ 2 = F_M^2(Q)S(Q). \qquad (11)$$

The difference of the two anisotropic terms is

$$\frac{d\sigma^-}{d\Omega}_{\text{aniso}} - \frac{d\sigma^+}{d\Omega}_{\text{aniso}} = 4F_N(Q)F_M(Q)S(Q) \qquad (12)$$

which arises from the interference between the nuclear and magnetic scattering amplitudes.

The spin dependent isotropic and anisotropic terms were obtained from the 2D scattering patterns with the BERSANS software package[24] which was also used to perform the standard data reduction procedure. Data reduction shows that there is a strong asymmetric $[d\sigma/d\Omega^-(Q) - d\sigma/d\Omega^+(Q)]$ scattering arising from the interference between the nuclear and magnetic scattering amplitudes. Figure 6 shows the iso-intensity plots for $[d\sigma/d\Omega^+ - d\sigma/d\Omega^-]$ on the xy detector. At higher applied magnetic fields, when moments are aligned along the field direction, a pronounced asymmetry is seen with almost zero intensity scattering along the direction of the applied field. This is an indication of the presence of a strong interference between nuclear and magnetic scattering amplitudes and highlights the power of polarized neutron for measuring weak magnetic scattering in presence of strong nuclear scattering and vice versa.[20]

The observed Q-dependent SANS data have been analyzed using the SASFIT software package developed at PSI
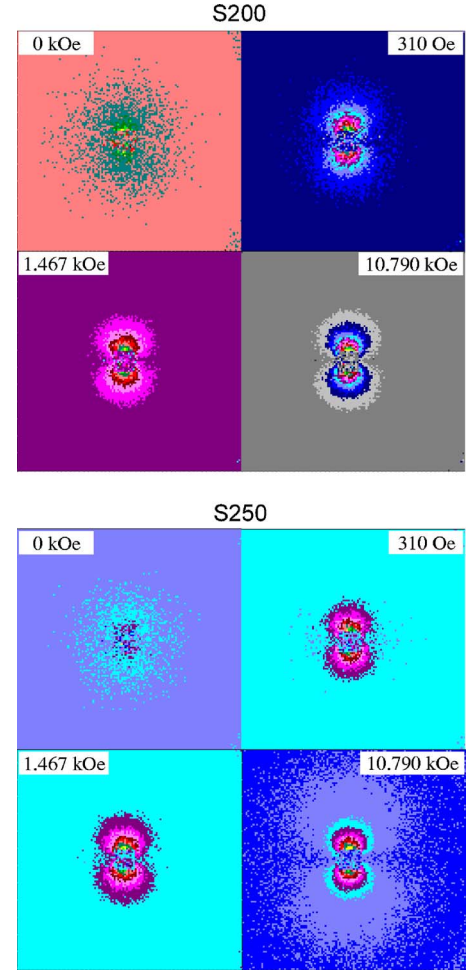

FIG. 6. (Color online) The iso-intensity plots of the observed difference SANS patterns $[d\sigma/d\Omega^+ - d\sigma/d\Omega^-]$ on the xy detector measured at room temperature in a horizontal magnetic field of 0, 0.310, 1.467, and 10.790 kOe, applied perpendicular to the incident polarized neutron beam at a sample to detector distance of 3 m for S200 and S250 samples.

for fitting analytical form factors simultaneously to several data sets. Figure 7 shows the experimental and theoretical curves for the $d\sigma/d\Omega^+_{\text{iso}}$, $d\sigma/d\Omega^-_{\text{iso}}$, $d\sigma/d\Omega^+_{\text{aniso}}$, and $d\sigma/d\Omega^-_{\text{aniso}}$ terms as a function of Q corresponding to $H = 10.79$ kOe. In order to show the difference between these curves prominently over the entire Q region, the y axis has been scaled with Q^2. It is evident that the isotropic terms for the flipper "off" and "on" states overlap each other, as expected from the theoretical formalism given above in Eq. (8). The neutron data corresponding to noninteracting magnetic nanoparticles have been analyzed using the formalism given by J. Kohlbrecher, A. Wiedenmann, and H. Wollenberger in Ref. 25. For the S200 sample, the nuclear scattering length density 7.17×10^{10} cm^{-2} was calculated from the chemical composition and the magnetic scattering length density 9.33×10^9 cm^{-2} was determined from a simultaneous fitting of the $d\sigma/d\Omega^+_{\text{iso}}(Q)$, $d\sigma/d\Omega^+_{\text{aniso}}(Q)$, $d\sigma/d\Omega^-_{\text{iso}}(Q)$, and $d\sigma/d\Omega^-_{\text{aniso}}(Q)$ data curves. Our experiments have given a direct confirmation of the log-normal number distribution of particle size. The solid lines in Fig. 7 are the best fit of the
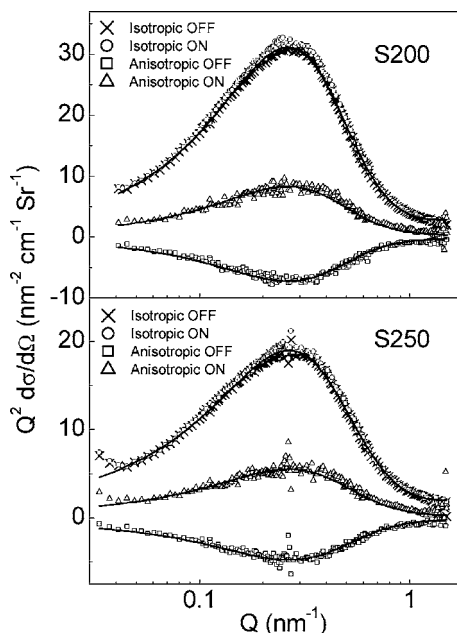
FIG. 7. Measured (symbols) and fitted (solid lines) isotropic and anisotropic parts of the $d\sigma/d\Omega^+_{iso}(Q)$, $d\sigma/d\Omega^+_{aniso}(Q)$, $d\sigma/d\Omega^-_{iso}(Q)$, and $d\sigma/d\Omega^-_{aniso}(Q)$ curves for the γ-Fe$_2$O$_3$ S200 and S250 samples.

data in this model. For the S250 sample, the nuclear scattering length density 7.17×10^{10} cm^{-2} and magnetic scattering length density 10.14×10^9 cm^{-2} are found. For the S250 sample, a slightly higher magnetic scattering is evident. The derived volume-weighted particle size distribution is depicted in Fig. 8. The median radii of 5.30 nm (distribution width=0.36) and 4.96 nm (distribution width=0.39) have been found, which correspond to median diameters of 10.60 and 9.92 nm for S200 and S250 samples, respectively. Figure 9 shows the experimental and calculated Q dependence of $[d\sigma/d\Omega^+(\mathbf{Q})-d\sigma/d\Omega^-(\mathbf{Q})]$, corresponding to the interference term between the nuclear and magnetic scattering amplitudes arising due to polarized neutron scattering, for both the samples. Figure 9 thus highlights the power of the polarized SANS experiments. The Shell model approach[20] consisting of a sphere of an inner core radius R surrounded by a concentric shell of radius ΔR was attempted for quantitative
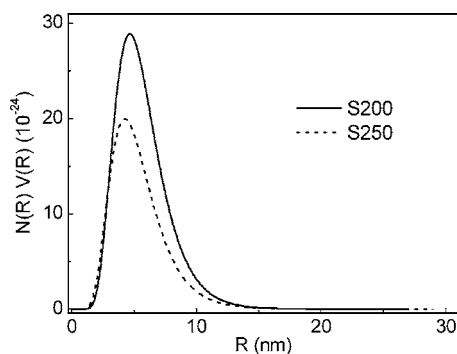

FIG. 8. Volume-weighted number distribution of particle size for the γ-Fe$_2$O$_3$ samples annealed at 200 and 250 °C, derived from SANS data.
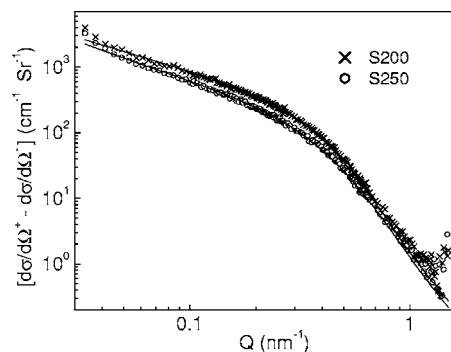

FIG. 9. Experimental (symbols) and calculated (solid lines) difference SANS patterns $[d\sigma/d\Omega^+ - d\sigma/d\Omega^-]$ as a function of Q for both the samples.

estimate of any possible surface disorder spins. However, within the sensitivity of the present polarized SANS study, the analysis did not show any magnetic dead layer at the surface of nanoparticles. In the present analysis we have therefore, adopted $f_p(\mathbf{Q})=f_m(\mathbf{Q})$ for spherical particle as per Eq. (4). Figure 10 shows the derived S(Q) which corresponds to interference effects caused by the actual dense spatial arrangement of nanoparticles. A mass fractal with a fractal dimension of 1.251 is found for both the samples. This means that the nanoparticles have certain tendency to form linear chains. One probable reason for this behavior is the dipolar magnetic field created by the magnetic nanoparticles. When the nanoparticles are synthesized, they have a certain spatial degree of freedom in the coalescence or aggregation process. In order to minimize the magnetostatic energy, it is favored to form chains with aligned nanoparticle magnetic moments. After synthesis, this tendency to form chains can be enhanced by application of magnetic fields if the nanoparticles are free to move.

Figure 11(a) depicts the zero-field-cooled (ZFC) and field-cooled (FC) dc magnetic susceptibility for the S200 sample. The ZFC and FC curves show a typical blocking process as reported for superparamagnetic (SPM) nanoparticles.[6,11,26,27] The blocking temperature T_B of SPM nanoparticles depends upon their size and crystalline anisotropy. The ZFC and FC curves can be used to find the distribution of blocking temperature in noninteracting nanoparticles systems.[28,29] Figure 11(b) shows the difference in ZFC
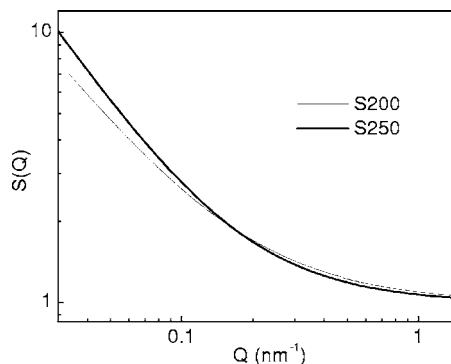

FIG. 10. Derived S(Q) for the γ-Fe$_2$O$_3$ samples annealed at 200 and 250 °C.

FIG. 12. Initial dc magnetization as a function of magnetic field at room temperature for the S200 sample. The solid curve is the theoretically fitted using the log-normal distribution of particle size (see text).
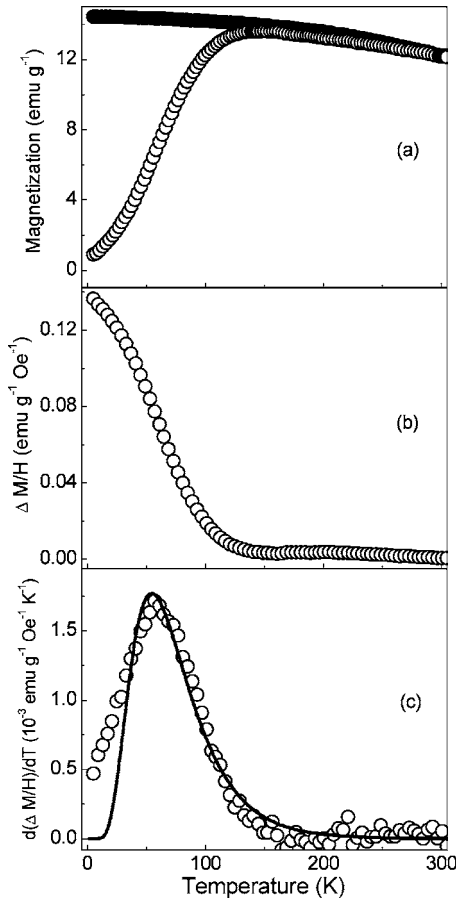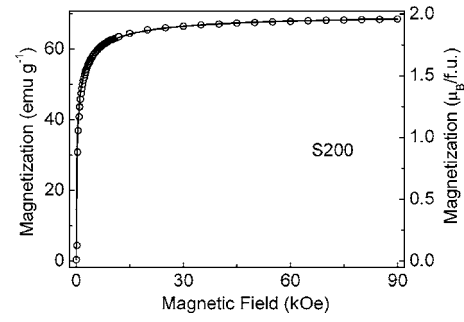

FIG. 11. (a) Temperature dependent dc susceptibility curves, ZFC (open symbols) and FC (solid symbols), measured under 100 Oe external field for the S200 sample. (b) The difference $\Delta M/H = (M_{FC} - M_{ZFC})/H$ between the ZFC and FC dc susceptibility curves as a function of temperature. (c) The derivative $d(\Delta M/H)/dT$ vs T fitted with the log-normal distribution function.

and FC magnetic susceptibility ($\Delta M/H$). The blocking temperature distribution can be obtained from the temperature derivative of the ($\Delta M/H$) vs T curves[28,29] (shown in the lower part of Fig. 11). This curve is fitted using the log-normal distribution function

$$f(T_B) = \frac{1}{\sqrt{2\pi}\sigma' T_B} \exp\left\{\frac{-[\ln(T_B/T_{BM})]^2}{2\sigma'^2}\right\}, \quad (13)$$

where T_{BM} is the median of blocking temperature and σ' is the distribution width. The log-normal fit yields the value of $T_{BM} \sim 67$ K with $\sigma' = 0.46$. A deviation in the fitted curve below ~ 35 K suggests the presence of interparticle interaction at low temperatures. Under the framework of the Néel superparamagnetic model,[30] at high temperatures, the magnetic moments of nanoparticles are free to respond to an external field, but at sufficiently low temperature, particle moments freeze. A freezing of particle moments over wide temperature range can be visualized in terms of a progressive blocking of nanoparticles-moments depending upon their volume V and magnetocrystalline anisotropy K. Below the freezing temperature, the particle moments freeze in random

orientations dictated by the magnetocrystalline anisotropy. Particles with larger KV freeze at higher temperature and the freezing temperature decreases with decreasing KV as per the Arrhenius law. Since at low temperatures, the magnetic moments of nanoparticles are frozen in an easy direction of magnetization, it gives rise to a low value of magnetization and at high temperatures, the magnetization decreases as T^{-1} due to thermal fluctuations of the magnetic moments. Therefore, a peak in the $M_{ZFC}(T)$ between these two temperature regions occurs.

Now we turn to the magnetization process $M(H)$ of these nanoparticles systems with particle size distribution. Figure 12 shows the virgin (initial) magnetization curve measured for the S200 sample at 297 K with a maximum magnetic field of 90 kOe. In order to gain a quantitative understanding of the nature of $M(H)$ behavior, we have analyzed the magnetization behavior under the framework of theory of superparamagnetism. In the SPM regime, the temperature and field dependence of the magnetization of an assembly of noninteracting SPM particles with uniform size can be described by[31]

$$M = M_S\left[\coth\left(\frac{\mu H}{kT}\right) - \frac{kT}{\mu H}\right] = M_S L\left(\frac{\mu H}{kT}\right), \quad (14)$$

where $L(x)$ is a Langevin function, M_S is the saturation magnetization, and μ is the magnetic moment of an individual SPM particle. If there is a distribution of size and hence moment, given by a distribution function $f(\mu)$, of SPM nanoparticle, the magnetization can be expressed as,[29,32]

$$M = M_S\int_0^\infty f(\mu)L\left(\frac{\mu H}{kT}\right)d\mu. \quad (15)$$

Assuming a log-normal distribution of the moments with median moment μ_m and width σ_2, $f(\mu)$ can be expressed as

$$f(\mu) = \frac{1}{\sigma_2\mu\sqrt{2\pi}} \exp\left\{\frac{-[\ln(\mu/\mu_m)]^2}{2\sigma_2^2}\right\}. \quad (16)$$

The calculated curve using Eq. (15) gives a good agreement with the experimental data with $\mu_m = 28\,000\ \mu_B$, a distribution width $\sigma_2 = 2.39$ and $M_S = 68.54$ emu/g ($\approx 1.96\ \mu_B$ per formula unit). The saturation magnetization M_S value is

found to be slightly higher as compared to the ordered net moment (~ 1.58 μ_B per formula unit) obtained from the neutron diffraction study. Here, we recall that the present neutron diffraction measurements were carried out in absence of external magnetic field. Therefore, the observed higher M_S value only indicates a possible field-induced effect on magnetization.

From the analysis of the $M(H)$ curve for the S200 sample, shown in Fig. 12, we can estimate the size of nanoparticles. The lattice constants, derived from the x-ray and neutron diffraction study, give a unit cell volume of 0.5798 nm^3. The theoretically expected spin only ordered moment for ferrimagnetic ordering between the tetrahedral and octahedral site moments is 2.5 μ_B per formula unit at 0 K. Since O^{2-} ions have no permanent magnetic moment, the ordered moment of γ-Fe_2O_3 originates from the moments of Fe^{3+} ions located at tetrahedral (A) and octahedral (B) sublattices of γ-Fe_2O_3 structure $(3/4)_A[5/4 \ \Box 1/4]_B$ O_3.[9] The numbers of filled tetrahedral and octahedral Fe^{3+} ions per formula unit are, therefore, 3/4 and 5/4. Fe^{3+} gives spin-only (orbital contribution quenched) ordered moment $\mu = g \ S \ \mu_B$ where Fe^{3+} carry $S = 5/2$, with g (the Lande g factor of the manganese ions) $=2$. Assuming complete ferrimagnetic alignment of the Fe^{3+} spins, a theoretical spin-only ordered moment of $[5/4 \times 2 \times 5/2$ (from octahedral site) $-3/4 \times 2 \times 5/2$ (from tetrahedral site)] $\mu_B = 2.5$ μ_B per formula unit is expected at 0 K. In γ-Fe_2O_3 structure since there are eight formula units of Fe_3O_4 (per unit cell) with 1/6 of the vacant octahedral sites, the theoretically expected spin-only ordered moment per unit cell is 26.67 μ_B. Therefore, the number of unit cells in a particle with moment 28 000 μ_B is 1050. Hence the volume of a particle [No. of unit cells × (volume of a unit cell)] is found to be 608.79 nm^3. Assuming particles with spherical shape (volume $V = \pi D^3/6$), particle diameter $D[=(6 \ V/\pi)^{1/3}]$ comes out to be 10.51 nm. Using the observed saturation moment M_S of 68.54 emu/g (≈ 1.96 μ_B per formula unit) the median particle diameter has been calculated to be ~ 11.4 nm. The particle size obtained from the M vs H fit is in good agreement with that obtained from the XRD, neutron diffraction, TEM, and SANS studies. Here we would like to comment on the derived apparently larger value of the distribution width $\sigma_2 = 2.39$. μ is directly proportional to volume of particle. On the other hand the log-normal distribution function used in the SANS data analysis as well as for the TEM study is in terms of radius of particles where one deals with "sigma radius." The distribution width for volume distribution of particles ("sigma volume") is theoretically three times larger than the "sigma radius." Taking this fact into account, from the $M(H)$ data the distribution width of radius of particles will be $\sigma_2' = \sigma_2/3 \approx 0.79$. However, this value is still larger than the distribution width of 0.39 obtained from the SANS studies and 0.19, obtained from the TEM studies. This could be due to the fact that SANS technique is known to be more sensitive on σ as the SANS signal is not proportional to V but V^2 ($\propto R^6$), the magnetization is on the other hand proportional to $V = R^3$. Another possible reason could be due to the presence of weak magnetic correlation between particle moments. In our analysis of M vs H data a noninteracting particle moment has been assumed.
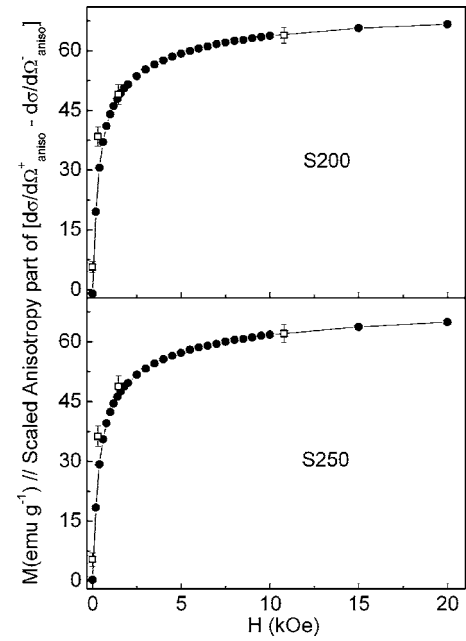

FIG. 13. Comparison of field dependence of the measured initial magnetization $M(H)$ and the $[d\sigma/d\Omega^+_{aniso} - d\sigma/d\Omega^-_{aniso}]$ SANS signal [Eq. (12)]. $[d\sigma/d\Omega^+_{aniso} - d\sigma/d\Omega^-_{aniso}]$ signal has been scaled at $H = 10.790$ kOe.

In Fig. 13, we compare the field dependence of dc magnetization and the integrated SANS intensity over the entire Q region of the difference of the two anisotropic scattering cross sections, i.e., $[d\sigma/d\Omega^+_{aniso} - d\sigma/d\Omega^-_{aniso}]$. Here the cross-section term $[d\sigma/d\Omega^+_{aniso} - d\sigma/d\Omega^-_{aniso}]$ is proportional the Langevin function. A very good one-to-one scaling, indicating the consistent behavior of field dependence of $F_M(\mathbf{Q})$ and dc magnetization M, is evident.

Nanoparticles of γ-Fe_2O_3 have been studied in great detail in the literature[10] due to their possible wide technological applications. However, to the best of our knowledge, the present study includes results of systematic measurements using a wide range of advanced techniques for the first time. The approach adopted in the present study gives a clear direction how to correlate various results that can be obtained on magnetic nanoparticle systems using different experimental techniques.

IV. SUMMARY AND CONCLUSION

We have carried out a detailed study of structural and magnetic properties at room-temperature for γ-Fe_2O_3 nanoparticles, an industrially important compound widely used for the production of magnetic recording materials, biomedical applications, and catalysis, by using high resolution TEM, electron energy loss spectroscopy (EELS), x-ray diffraction, neutron diffraction, polarized SANS, and dc magnetization techniques. The results of these experiments have given a direct understanding on the size and shape of particles, distribution of particle size, their structural correlation, detailed nature of crystallinity, and magnetic properties. The present study deals with an important problem of the sym-

TABLE IV. Particle diameter with error bars for γ-Fe_2O_3 nanoparticles determined using various techniques. Details are given in the text.

Sample	TEM (nm)	XRD (nm)	ND (nm)	SANS (nm)	$M(H)$ (nm)
S200	8.6(0.19)	11.6(0.1)	11.6(0.8)	10.60(0.36)	11.4(0.8)
S250	10.17(0.27)	11.3(0.2)	11.2(0.5)	9.92(0.39)	—

metry (space group) of γ-Fe_2O_3 nanoparticles as well as that of the character of cation lattice vacancy distribution. The crystal structure is found to be consistent with P4$_3$ 3 2 space group with cation vacancies at the 12*d* and 4*b* octahedral sites (9.75 and 37.5 at. %, respectively, for the sample annealed at 200 °C). γ-Fe_2O_3 being a very important material with wide commercial and industrial applications, the knowledge of such microstructure of this material is of much interest. A log-normal distribution of particle size is found in TEM, polarized SANS, as well as $M(H)$ investigations and the derived distribution parameters, obtained from these studies, are in good agreement (see Table IV). Neutron diffraction study confirms a ferrimagnetic ordering of tetrahedral and octahedral site moments with a net moment of $\sim$1.58 and 1.83 μ_B per formula unit for the samples annealed at 200 and 250 °C, respectively. Here we would like to mention that the neutron diffraction measurements have been carried out at room temperature (297 K). Whereas, one expects 5 μ_B spin-only magnetic moment for Fe^{3+} only at 0 K. Therefore, a lower observed moment at 297 K as compared to 0 K is expected. In addition to this it is possible that surface spins are canted (disordered) and cause a reduction in the net moment. However, SANS study does not show any clear evidence (within its detection limit) of the presence of any layer of disordered surface spins. The magnetic signal has been measured with a greater sensitivity through the interference term between the magnetic and nuclear scattering amplitudes in our polarized SANS study. SANS data have been analyzed assuming the same form factor for spherical particles for both nuclear and magnetic scattering. SANS data analysis is consistent with a mass fractal spatial arrangement of these nanoparticles with a fractal dimension of 1.25. Superparamagnetic behavior of these nanoparticles at room temperature with a particle moment of $\sim$28 000 μ_B without any magnetic interaction between these nanoparticles is found in our dc magnetization study. The blocking temperatures of these nanoparticles are found to obey a log-normal distribution function. By studying two samples prepared in the similar way, but with different annealing temperatures of 200 and 250 °C, we have shown that the observed structural and magnetic results are inherent of γ-Fe_2O_3 and very much reproducible.

In the present study, we have found a maximum magnetization of $\sim$68.5 emu g^{-1} (1.98 μ_B/f.u.) at 297 K under 90 kOe field. This value is quite close to theoretically expected saturation magnetization of 2.5 μ_B/f.u. at T=0 K for bulk γ-Fe_2O_3. For the present system, observed magnetization is significantly higher than that (52.78 emu g^{-1}) reported in the literature.[33] The observed high value of magnetization with significantly low technical saturation applied field (with

strong ferrimagnetic character) at room temperature and low blocking temperature ($\sim$67 K) make the studied material more attractive for practical applications in drug delivery. Though in an earlier study a relatively large value of magnetization was reported for "nearly-defect-free" γ-Fe_2O_3 nanocrystallites,[12] no detailed quantitative structural analysis was given in that study. Such quantitative analysis is very much necessary in view of the dependence of magnetic properties on atomic/vacancies distribution in this system with cation vacancy. The present paper therefore, fills the gap in this respect. The present paper also deals with the quantitative analysis of distribution of particles size using various advanced techniques and its implications in establishing the magnetic properties [$M(H)$ and blocking temperature distribution]; a very important aspect in the area of nanoscience and nanotechnology. The existence of surface spin disorder and its possible role on magnetic properties are important issues in nanoscience. A very small (6 Å) surface spin disorder in γ-Fe_2O_3 nanoparticles has been reported by non-neutron techniques in the literature.[34] However, in the present study we have not found any evidence of surface spin disorder, which, if existing, has to be below the sensitivity level of the polarized SANS technique. In fact, the same value of grain size and magnetic domain size are found to represent well the neutron diffraction data. The grain size obtained from neutron study is consistent with that from the x-ray diffraction study. High resolution TEM study also does not show any density variation near the surface. This paper, using various techniques, gives a synergetic view of the distribution of particle size that is often obtained in an isolated manner by limited number of techniques on a given nanoparticle system in the literature. We believe the results of the present systematic study using various advanced techniques will be useful to researchers working in the area of nanoscience and nanotechnology.

*Corresponding author. FAX: +91 22 25505151; Electronic address: smyusuf@barc.gov.in

[1] A. Moser, K. Takano, D. T. Margulies, M. Albrecht, Y. Sonobe, Y. Ikeda, S. Sun, and E. E. Fullerton, J. Phys. D **35**, R157 (2002).

[2] *Handbook of Advanced Magnetic Materials: Vol 4. Properties and Applications*, edited by Y. Liu, D. J. Sellmyer, and D. Shindo (Spinger, Berlin, 2006).

[3] K. J. Kirk, Contemp. Phys. **41**, 61 (2000).

[4] R. D. McMichael, R. D. Shull, L. J. Swartzendruber, and L. H. Bennett, J. Magn. Magn. Mater. **111**, 29 (1992).

[5] J. Popplewel and L. Sakhnini, J. Magn. Magn. Mater. **149**, 72 (1995).

[6] R. D. Ambashta, S. M. Yusuf, M. D. Mukadam, S. Singh, P. K Wattal, and D. Bahadur, J. Magn. Magn. Mater. **293**, 8 (2005).

[7] S. R. Rudge, T. L. Kurtz, C. R. Vessely, L. G. Catterall, and D. L. Williamson, Biomaterials **21**, 1411 (2000).

[8] O. M. Koo, I. Rubinstein, and H. Onyuksel, Nanomedicine: Nanotechnology, Biology, and Medicine **1**, 193 (2005).

[9] C. Greaves, J. Solid State Chem. **49**, 325 (1983).

[10] J. L. Dormann, F. D'Orazio, F. Lucari, E. Tronc, P. Prené, J. P. Jolivet, D. Fiorani, R. Cherkaoui, and M. Noguès, Phys. Rev. B **53**, 14291 (1996); S. Mørup, E. Tronc, E. Schmidbauer, and R. Keller, J. Magn. Magn. Mater. **152**, 99 (1996); S.-J. Lee, J.-R. Jeong, S.-C. Shin, J.-C. Kim, and J.-D. Kim, *ibid.* **282**, 147 (2004); S. Brice Profeta, M.-A. Arrio, E. Tronc, N. Menguy, I. Letard, C. Cartier dit Moulin, C. Noguès, C. Chaneac, J.-P. Jolivet, and Ph. Sainctavit, *ibid.* **288**, 354 (2005); F. Gazeau, J. C. Bacri, F. Gendron, R. Perzynski, Yu. L. Raikher, V. I. Stepanov, and E. Dubois, *ibid.* **186**, 175 (1998); J. Z. Jiang, J. Staun Olsen, L. Gerward, and S. Mørup, Europhys. Lett. **44**, 620 (1998); M. P. Morales, C. J. Serna, F. Bødker, and S. Mørup, J. Phys.: Condens. Matter **9**, 5461 (1997); X. Ye, D. Lin, Z. Jiao, and L. Zhang, J. Phys. D **31**, 2739 (1998).

[11] M. D. Mukadam, S. M. Yusuf, P. Sharma, and S. K. Kulshreshtha, J. Magn. Magn. Mater. **272-274**, 1401 (2004).

[12] P. Dutta, A. Manivannan, M. S. Seehra, N. Shah, and G. P. Huffman, Phys. Rev. B **70**, 174428 (2004).

[13] G. A. Ferguson, Jr. and M. Hass, Phys. Rev. **112**, 1130 (1958).

[14] M. Boudeulle, H. Batis-Landoulsi, Ch. Leclercq, and I. Vergnon, J. Solid State Chem. **48**, 21 (1983).

[15] K. Haneda and A. H. Morrish, Solid State Commun. **22**, 779 (1977).

[16] K. M. Lee and C. M. Sorensen, IEEE Trans. Magn. **28**, 3180 (1992); M. P. Pileni, Langmuir **13**, 3266 (1997).

[17] C. Frandsen, C. R. H. Bahl, B. Lebech, K. Lefmann, L. Theil Kuhn, L. Keller, N. H. Andersen, M. v. Zimmermann, E.

Johnson, S. N. Klausen, and S. Mørup, Phys. Rev. B **72**, 214406 (2005).

[18] T. Roisnel and J. Rodriguez-Carvajal, WINPLOTR: A Windows tool for powder diffraction patterns analysis, *Materials Science Forum, Proceedings of the Seventh European Powder Diffraction Conference (EPDIC 7)*, 2000, p. 118–123, edited by R. Delhez and E. J. Mittenmeijer; J. Rodriguez-Carvajal and T. Roisnel, FULLPROF.98 and WINPLOTR: New Windows 95/NT Applications for Diffraction Commission For Powder Diffraction, International Union for Crystallography, *Newletter N_20 (May-August) Summer 1998*.

[19] N. Shmakov, G. N. Kryukova, S. V. Tsibula, A. I. Chuvilin, and L. P. Solovyeva, J. Appl. Crystallogr. **28**, 141 (1995); Z. Somogyvári, E. Sváb, G. Mészáros, K. Krezhov, I. Nedkov, I. Sajó, and F. Bourée, Appl. Phys. A: Mater. Sci. Process. **74**, S1077 (2002); A. N. Shmakov, G. N. Kryukova, S. V. Tsybulya, A. L. Chuvilin, and L. P. Solovyeva, J. Appl. Crystallogr. **28**, 141 (1995).

[20] W. Wagner and J. Kohlbrecher, in *Modern Techniques for Characterizing Magnetic Materials*, edited by Y. Zhu (Springer, Berlin, 2005), ISBN: 14020-8007-7.

[21] A. Wiedenmann, Physica B **356**, 246 (2005).

[22] I. Bergenti, A. Deriu, L. Savini, E. Bonetti, and A. Hoell, J. Appl. Crystallogr. **36**, 450 (2003).

[23] A. Hoell, A. Wiedenmann, U. Heyen, and D. Schüler, Physica B **350**, e309 (2004).

[24] BERSANS: SANS data reduction software, Uwe Keiderling (HMI, Berlin), 1994–2000.

[25] J. Kohlbrecher, A. Wiedenmann, and H. Wollenberger, Z. Phys. B: Condens. Matter **104**, 1 (1997).

[26] N. K. Prasad, D. Panda, S. Singh, M. D. Mukadam, S. M. Yusuf, and D. Bahadur, J. Appl. Phys. **97**, 10Q903 (2005).

[27] M. Mandal, S. Kundu, S. K. Ghosh, S. Panigrahi, T. K. Sau, S. M. Yusuf, and T. Pal, J. Colloid Interface Sci. **286**, 187 (2005).

[28] J. C. Denardin, A. L. Brandl, M. Knobel, P. Panissod, A. B. Pakhomov, H. Liu, and X. X. Zhang, Phys. Rev. B **65**, 064422 (2002).

[29] M. D. Mukadam, S. M. Yusuf, P. Sharma, and S. K. Kulshreshtha, J. Magn. Magn. Mater. **269**, 317 (2004).

[30] L. Neel, Ann. Geophys. (C.N.R.S.) **5**, 99 (1949).

[31] C. P. Bean and J. D. Livingston, J. Appl. Phys. **30**, 120S (1959).

[32] F. C. Fonseca, A. S. Ferlauto, F. Alvarez, G. F. Goya, and R. F. Jardim, J. Appl. Phys. **97**, 044313 (2005).

[33] D. Chen and R. Xu, J. Solid State Chem. **137**, 185 (1998).

[34] B. Martínez, X. Obradors, Ll. Balcells, A. Rouanet, and C. Monty, Phys. Rev. Lett. **80**, 181 (1998).